electronic materials

MDPI

Article

Synthesis and Physical Properties of Iridium-Based Sulfide $Ca_{1-x}Ir_4S_6(S_2)$ [x = 0.23–0.33]

Michael Vogl [1,*], Martin Valldor [1,2,*], Roman Boy Piening [1], Dmitri V. Efremov [1], Bernd Büchner [1,3] and Saicharan Aswartham [1,*]

[1] Institut für Festkörperforschung, Leibniz IFW Dresden, Helmholtzstraße 20, 01069 Dresden, Germany; B.Piening@web.de (R.B.P.); d.efremov@ifw-dresden.de (D.V.E.); B.Buechner@ifw-dresden.de (B.B.)
[2] Department of Chemistry, University of Oslo, N-0315 Oslo, Norway
[3] Institut für Festkörper- und Materialphysik and Würzburg-Dresden Cluster of Excellence ct.qmat, Technische Universität Dresden, 01062 Dresden, Germany
* Correspondence: m.vogl@ifw-dresden.de (M.V.); b.m.valldor@kjemi.uio.no (M.V.); s.aswartham@ifw-dresden.de (S.A.)

Abstract: We present the synthesis and characterization of the iridium-based sulfide $Ca_{1-x}Ir_4S_6(S_2)$. Quality and phase analysis were conducted by means of energy-dispersive X-ray spectroscopy (EDXS) and powder X-ray diffraction (XRD) techniques. Structure analysis reveals a monoclinic symmetry with the space group $C\,1\,2/m\,1$ (No. 12), with the lattice constants a = 15.030 (3) Å, b = 3.5747 (5) Å and c = 10.4572 (18) Å. Both X-ray diffraction and EDXS suggest an off-stoichiometry of calcium, leading to the empirical composition $Ca_{1-x}Ir_{4.0}S_6(S_2)$ [x = 0.23–0.33]. Transport measurements show metallic behavior of the compound in the whole range of measured temperatures. Magnetic measurements down to 1.8 K show no long range order, and Curie–Weiss analysis yields $\theta_{CW} = -31.4$ K, suggesting that the compound undergoes a magnetic state with short range magnetic correlations. We supplement our study with calculations of the band structure in the framework of the density functional theory.

Keywords: solid-state synthesis; X-ray diffraction; band structure; magnetic measurements

Citation: Vogl, M.; Valldor, M.; Piening, R.B.; Efremov, D.V.; Büchner, B.; Aswartham, S. Synthesis and Physical Properties of Iridium-Based Sulfide $Ca_{1-x}Ir_4S_6(S_2)$ [x = 0.23–0.33]. *Electron. Mater.* **2022**, *3*, 41–52. https://doi.org/10.3390/electronicmat3010004

Academic Editor: Jung-Hun Seo

Received: 19 November 2021
Accepted: 4 January 2022
Published: 11 January 2022

1. Introduction

The recent materials synthesis and investigation of sulfur-based compounds have shown the presence of exotic insulating ground states, sometimes accompanied by charge density wave and superconducting transitions. For example, $BaNiS_2$ [1] shows a metal-insulator transition (MIT). This MIT has attracted interest because it is associated with a competition between an insulating antiferromagnetic (AF) phase and a paramagnetic metallic one [2], similar to the case of unconventional superconductors, such as cuprates [3], Fe-based [4], and heavy fermions [5], whereas $BaFe_2S_3$ is a Mott insulator that shows a stripe-type magnetic order below 119 K [6]. In addition, ternary metal sulfides, such as $NiCo_2S_4$, have received attention for their catalytic activity in oxygen reduction and evolution reactions [7,8].

Most of these materials are 3*d*-based sulfur compounds. There are only a few examples of 5*d*-based, especially Ir-based, compounds, one of which is the spinel structure type $CuIr_2S_4$ that has a mixed Ir^{3+}/Ir^{4+} metallic phase and undergoes a first-order transition near 230 K to a low-temperature, charge-ordered, diamagnetic, insulating phase [9–11]. In general, 5*d*-transition metal ions possess a unique combination of spin-orbit coupling, coulomb interactions, and crystal field splitting, which may lead to unique and novel physical properties [12,13]. Iridium in particular has received a lot of attention. For example, it has been used to study the magnetic properties of the geometrically frustrated honeycomb-lattice in Li_2IrO_3 and Na_2IrO_3 [14,15], as well as a variety of compounds of the perovskite [16–19] and pyrochlore [20,21] families.

However, while numerous iridium oxides are known and investigated [12,20], the combination of iridium ions coordinated by sulfur is so far largely unexplored. In particular, ternary phases containing iridium, sulfur, and an alkaline or alkaline earth metal are unknown. One possible reason for this is that the chemical nature of sulfur is considerably different from oxygen, due to its high tendency to form polysulfides [22–25]. This often makes the synthesis of new sulfides by simple substitution of oxygen in known oxides difficult or even impossible.

Motivated by this, we performed exploratory chemistry within ternary and quaternary phase diagrams including the elements iridium and sulfur, which lead to the discovery of the previously unknown compound $Ca_{1-x}Ir_4S_6(S_2)$, which is described below. To our best knowledge, this is the first ternary compound in the calcium-iridium-sulfur phase diagram.

2. Experimental Section

All procedures for the preparation of the reaction mixture were performed in a glove box in an atmosphere of dry argon. For the synthesis of $Ca_{1-x}Ir_4S_8$, 0.045 g CaS (Alfa Aesar, 99.9%), 0.484 g Ir-metal powder (evochem, 99.9%), and 0.141 g elemental sulfur (Alfa Aesar, 99.5%) were mixed and ground. The powder was filled into an alumina-crucible which was placed in a quartz ampule with a length of 10–15 cm and an inner diameter of 0.8–1.2 cm. The ampule was then evacuated to a pressure of 10^{-5} mbar and then sealed under partial argon pressure. Then, the sealed ampule was placed in a box furnace and heated to 900 °C with a heating rate of 150 °C/h. The temperature was kept for 60 h, followed by a cooling to room temperature with a rate of 150 °C/h. After one regrinding step, the annealing was repeated for another 40 h at 900 °C. Following the two steps at 900 °C, the reaction temperature was gradually increased to improve sample quality. The sample was heated to 1000 °C, 1100 °C, and 1150 °C each for 50 h, with similar heating and cooling rates as for the previous steps at 900 °C. The product was obtained as a dark grey, well-sintered powder.

Powder X-ray diffraction (XRD) was performed using the transmission method on a StoeStadi-Powder diffractometer (STOE & Cie GmbH, Damstadt, Germany) with Mo-Kα and Co-Kα radiation, and at DESY High Resolution Powder Diffraction Beamline P02.1. For the Rietveld-refinement, the software package FullProf and JANA2006 was used [26–28]. The actual composition of the as-synthesized polycrystalline sample was determined by using an X-ray energy-dispersive spectrometer (INCA X-sight, Oxford Instruments, Abingdon, UK) mounted on a field-emission scanning electron microscope JEOL JSM 6490 LV with a W-cathode. A quantitative analysis of the spectra was performed using the INCA software (Oxford Instruments). Elemental analysis of the Ca content was performed via inductively coupled plasma optical emission spectrometry (ICP-OES) on an iCAP 6500 Duo View spectrometer (Thermo Fisher Scientific, Waltham, MA, USA). Prior to the analysis, the Ca was extracted by alkaline chemical digestion.

Temperature- and field-dependent magnetization studies were performed using a commercial Superconducting Quantum Interference Device (SQUID) magnetometer by Quantum Design (MPMS-XL SQUID-magnetometer, Quantum Design, San Diego, CA, USA). The electrical resistivity measurements were carried out by using a standard four-point technique in a homebuilt dip stick from room temperature down to 4.8 K. Silver wires were electrically connected to the sample surface with silver paint on a pressed pellet with a four-point contact method.

3. Results

3.1. Synthesis

In an attempt to investigate tertiary phases containing calcium, iridium and sulfur, a mixture of CaS, iridium metal and sulfur with the stoichiometry Ca:Ir:S = 1:1:3 reacted at 900 °C. A phase of said composition could not be found. However, amongst residues of the starting materials, the pattern of an unknown structure was found by X-ray diffraction. Via EDX spectroscopy, the composition of this previously unknown phase was determined to be Ca:Ir:S $\approx$ 1:4:8.

In the following, a phase-pure synthesis of this compound was attempted. The key finding, which made the synthesis of the material possible, was the optimization of the temperature profile. Several sintering temperatures were tested. At 800 °C, no complete reaction occurred. Significant amounts of the educts were still detectable in XRD. Through the reaction at 900 °C, the main phase formed in relatively pure form, but a small peak of unknown origin was visible at $1/d \approx 0.334$ Å^{-1} (Figure 1) as well as traces of small amounts of leftover iridium metal and CaS. The peak at 0.334 Å^{-1} disappeared after reannealing the sample at 1000 °C; however, even after two more annealing steps at 1100 °C and 1150 °C, small traces of the starting materials remained in the sample.

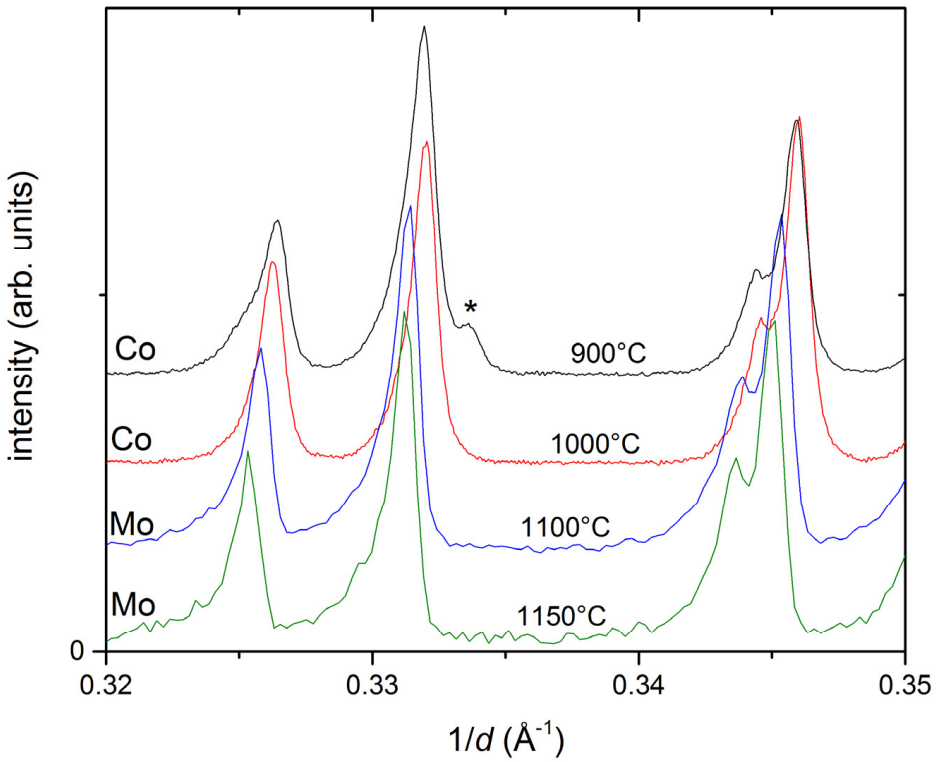

Figure 1. Powder X-ray diffraction data of $Ca_{1-x}Ir_4S_6(S_2)$ as obtained from samples reacted at different temperatures. Co and Mo indicate which samples were measured with Co-Kα or Mo-Kα radiation, respectively. The impurity peak from the reaction at 900 °C is marked with *.

SEM and EDXS analysis were also performed on the as-synthesized polycrystalline sample. The chemical composition was measured at 23 points of the sample, yielding the empirical composition $Ca_{0.75\pm0.05}Ir_{4.00\pm0.20}S_{8.12\pm0.98}$, indicative of substantial Ca-deficiency. The rough sample surface may as well have contributed to the deviations from the nominal composition. We have also analyzed the Ca-content by inductively coupled plasma atomic emission spectroscopy (ICP-OES). The measured calcium content is 2.92 $\pm$ 0.15 m%, which corresponds to $Ca_{0.77\pm0.04}Ir_4S_8$. It agrees quite well with the EDX estimation of calcium ($Ca_{0.75}$) within the error bars.

In order to reduce the remaining impurities, the synthesis of $Ca_{1-x}Ir_4S_8$ was also attempted with calcium-deficient starting compositions, specifically with Ca:Ir:S ratios of 0.9:4:8 and 0.8:4:8. For these synthesis attempts, a similar procedure and heating profile was used as described above. However, the phase purity of the target phase could not be improved in this way. Instead, additional secondary phases, such as IrS_2, were detected via XRD.

The $Ca_{1-x}Ir_4S_8$ sample obtained after reaction at 1150 °C was chosen for further investigations. Air sensitivity was tested by exposure overnight. The X-ray diffraction

pattern remained unchanged. Additionally, an XRD measurement at 13 K revealed no temperature dependent structural phase transitions.

Under the same reaction conditions, the synthesis of other similar materials with the stoichiometry CaM_4S_8 with different metals was attempted, namely M = Rh, In, Sb, Ru. These were chosen due to their ability to adopt a M^{3+} oxidation state and their ionic radii being close to that of iridium. However, the synthesis attempts either only yielded the binary sulfides or no reaction occurred. No ternary phases were observable in X-ray diffraction measurements.

3.2. Structure Description

For an in-depth study of the crystal structure of $Ca_{1-x}Ir_4S_8$, an XRD measurement with synchrotron radiation (λ = 0.20715 Å) was performed (Figure 2). The refinement was carried out in space group *C* 1 2/*m* 1. The resulting data, as obtained by JANA2006, are presented in Table 1. The iridium-lattice is built up by triangular layers propagating along the *b*-axis, which are folded to form tunnels (Figure 3). All iridium-ions are six-fold coordinated by regular sulfur S^{2-} and $(S_2)^{2-}$ pairs in distorted octahedra, with the Ir–S distances in the range of 2.316–2.402 Å (Figure 4a). In comparable Ir^{3+}-sulfides, distances are similar. For comparison, the S–S distance in IrS_2, which should in fact be written as $Ir_2S_2(S_2)$, is 2.30 Å [29]. It is discussed as being closely related to the observed small band-gap semiconducting properties. Slightly shorter S–S distances are known from other persulfide compounds like pyrite FeS_2 (2.177 Å) [22] and K_2S_2 (2.102 Å) [23]. Hence, $Ca_{1-x}Ir_4S_8$ has to be written as $Ca_{1-x}Ir_4S_6(S_2)$. The octahedra are edge-sharing along the triangular iridium layers. In contrast, inter-layer connections comprise corner sharing. This intimate connectivity between Ir-S-octahedra is also observed in $Ir_2S_2(S_2)$ [29], suggesting high stability of this arrangement.

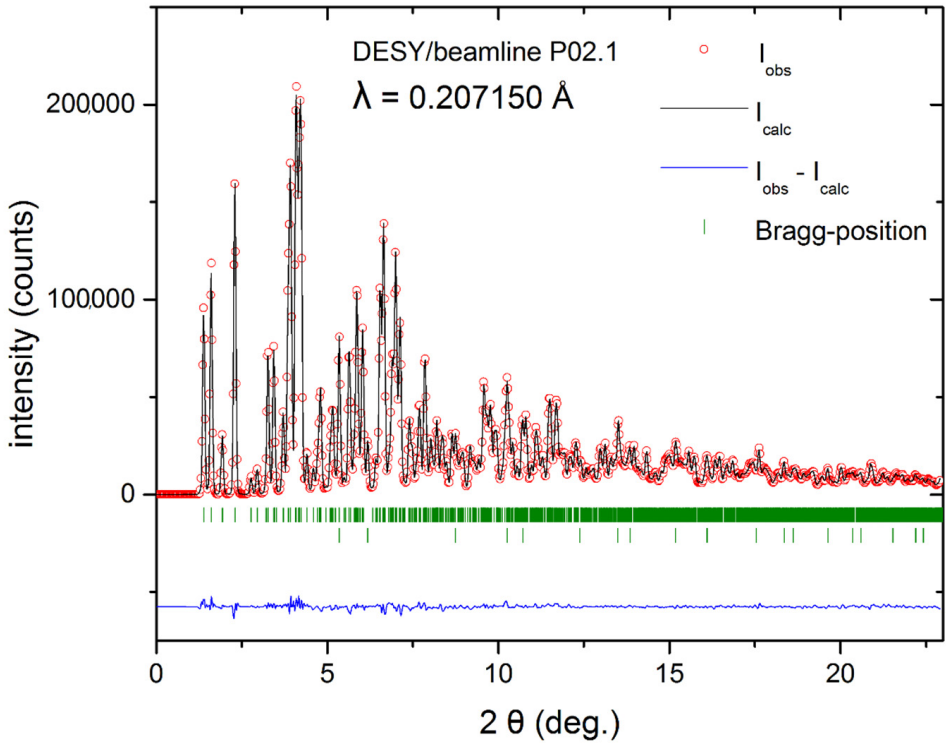

Figure 2. Rietveld-refinement of the powder diffraction pattern of $Ca_{1-x}Ir_4S_6(S_2)$ obtained with synchrotron radiation.

Table 1. Crystal structure data for $Ca_{1-x}Ir_4S_6(S_2)$ obtained from JANA2006 refinement. The refined crystal structure model and the powder X-ray diffraction presented here are available in CCDC: Deposition Number 2128279.

Parameters	Temperature (K)	293
	Wavelength λ/Å	0.20715
	2θ range/°	0.0114–22.9118
Crystal Data	Space group	*C* 1 2/*m* 1 (12)
	a/Å	15.030 (3)
	b/Å	3.5747 (5)
	c/Å	10.4572 (18)
	α/°	90
	β/°	124.970 (9)
	γ/°	90
	V/Å^3	460.39 (15)
Refinement	Goodness-Of-Fit	8.87
	Refined parameters	44
	Profile type	Pseudo-Voigt
	wR_p	0.0437
	R_F	0.0294

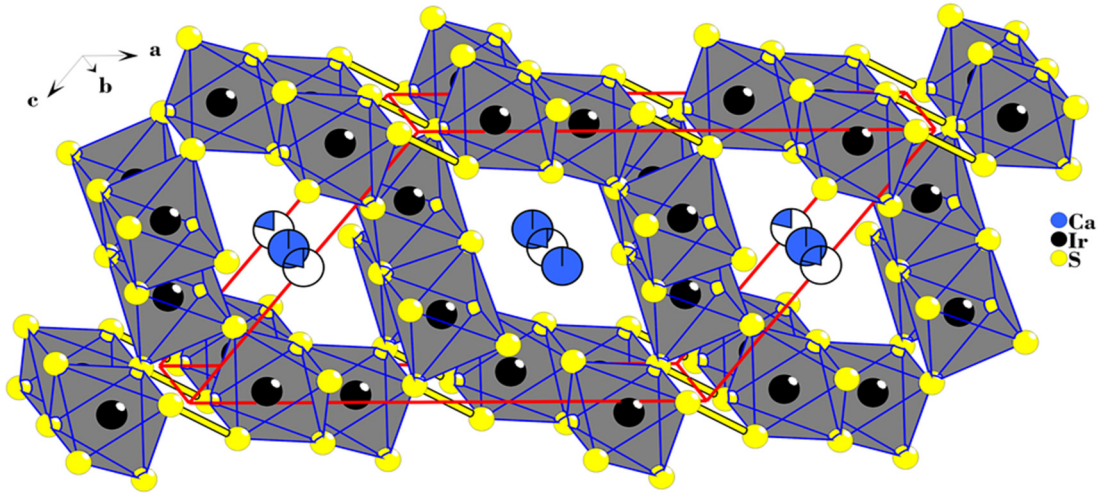

Figure 3. Crystal structure of $CaIr_4S_6(S_2)$ viewed along the b-axis.

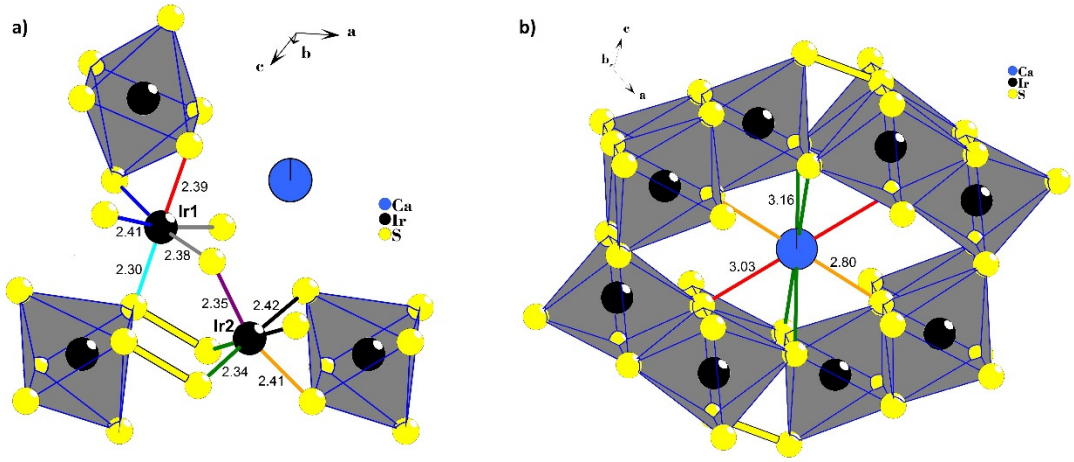

Figure 4. Ir (**a**) and Ca (**b**) coordination in $CaIr_4S_6(S_2)$ with bond lengths in Å. Bonds shown in the same color have the same length.

The Ca-cations are sitting in the voids formed by the tunnels of the Ir-S lattice and form one-dimensional chains along the *b*-axis (Figure 4b). From the Rietveld simulation, it is obvious that Ca is site-disordered: two split-positions with different occupancies, set as free parameters during the refinement, are needed to reach a satisfying model. As a result of site disorder and low occupancy, the Ca-S distances are somewhat longer (2.84–3.20 Å; Figure 4b) than those in CaS (2.85 Å). The resulting occupancies suggest a stoichiometry of $Ca_{1-x}Ir_4S_6(S_2)$ ($x \approx 0.33$), agreeing approximately with the EDXS data. Furthermore, the high B_{iso} values suggest delocalization or even mobility of the Ca-cations along the *b*-axis. For charge neutrality, it is expected that, in part, magnetic Ir^{4+} is present. Similar static disorder and split positions are commonly used to describe atomic disorder in tunnel structures, for example in $K_{1+x}Mo_{12}S_{14}$ (x = 0, 1.1, 1.3, and 1.6) [30] and hollandite $K_{1.33}Mn_8O_{16}$, $PbIr_4Se_8$ [31,32].

The structural similarities between the title compound and $Ir_2S_2(S_2)$ are obvious. In $Ir_2S_2(S_2)$, there are extended voids with walls consisting of six octahedra. However, in $Ca_{1-x}Ir_4S_8$, the presence of Ca causes the tunnels to expand and have eight octahedra in the walls.

3.3. Magnetic Investigation

The temperature dependence of magnetization of $Ca_{1-x}Ir_4S_6(S_2)$ in the range 1.8–300 K is measured and is shown in Figure 5a. It increases with the lowering of the temperature, showing a typical paramagnetic behavior. By measuring in several different fields, the presence of a minor ferromagnetic secondary phase is suggested because higher fields saturate the effect of the extrinsic signal. By Curie–Weiss approximation on the low field data, the magnetic moment per formula unit is estimated to μ_{eff} = 0.4 μ_B.

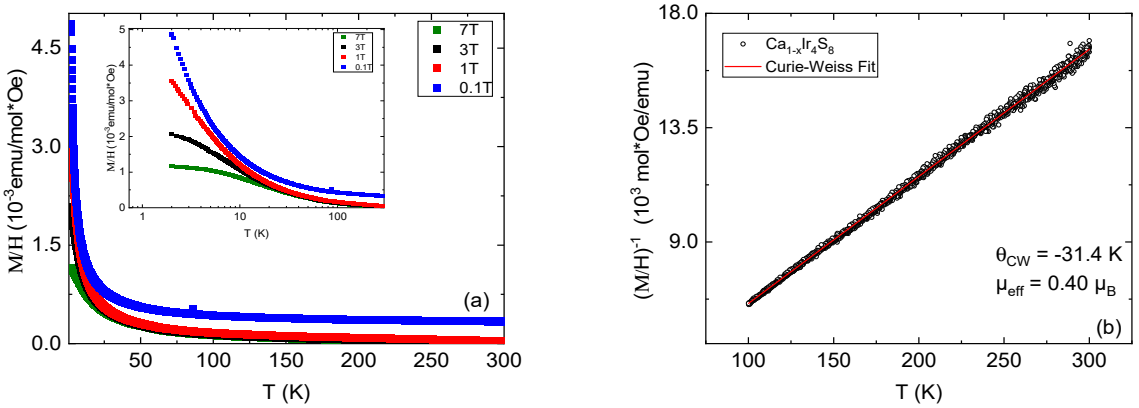

Figure 5. (**a**) Magnetization as a function of temperature for $Ca_{1-x}Ir_4S_8$ at different magnetic fields. Inset shows the logarithmic scale at low temperature; (**b**) Curie–Weiss analysis.

Iridium ions in the parent compound $Ca^{2+}Ir^{3+}{}_4S^{2-}{}_6(S_2)^{2-}$ have electronic configuration $5d^6$. The crystal field splits the electrons onto duplet e_g and triplet t_{2g} orbitals as $e_g{}^0t_{2g}{}^6$, which corresponds to a nonmagnetic ion S = 0. However, the doping by the Ca vacancies leads to the mixed valence state Ir^{3+}/Ir^{4+}. Assuming a fully localized picture, the observed value of magnetic moment per formula of 0.4 μ_B is small. This potentially indicates a lower Ca deficiency (x = 0.025). Another common cause for a decreased value of μ_{eff} is the presence of itinerant electrons that do not contribute to the effective magnetic moment. Given the metallic properties of $Ca_{1-x}Ir_4S_6(S_2)$ (see Section 3.4), this is the most likely explanation.

The Curie–Weiss temperature obtained from the fit is $\theta_{CW} = -31.4$ K. A negative value is typical for localized spins with antiferromagnetic interactions. However, in $Ca_{1-x}Ir_4S_6(S_2)$, no signs of long-range magnetic order are found.

3.4. Electrical Transport

The temperature dependent electrical transport of $Ca_{1-x}Ir_4S_6(S_2)$ in the range from 4.8 K to 300 K is shown in Figure 6. The electrical resistivity decreases as a function of temperature, clearly showing the metallic nature of the sample. The temperature-dependence is nonlinear. Our analysis yields a power law behavior $\rho = (\rho_0 + AT^2)$. In the interval 0–300 K, the resistivity increases by 30% only. It indicates the dirty metal behavior.

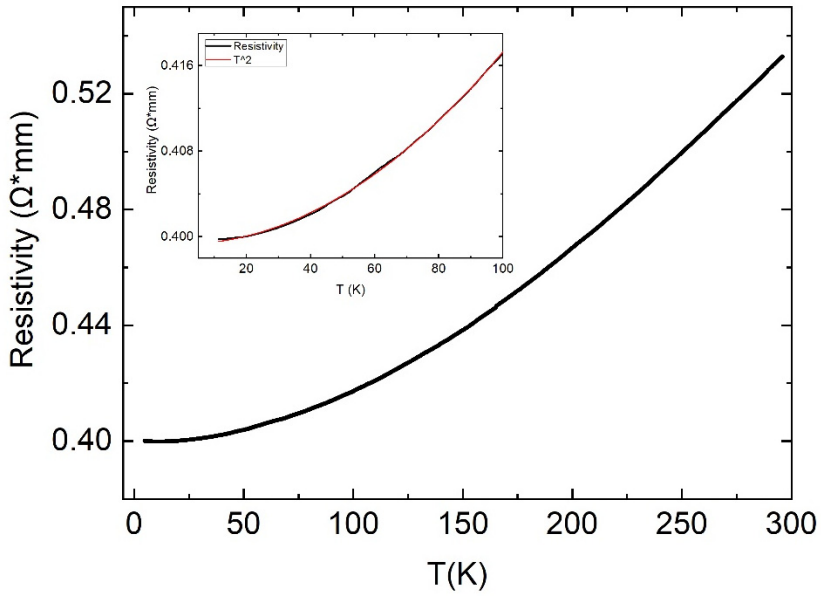

Figure 6. Electrical resistivity of $Ca_{1-x}Ir_4S_8$. The inset shows the low-temperature data which can be well fitted with a quadratic power law, as is typical for metallic materials.

3.5. Electronic Band Structure Calculation

To get some insights about the ground state, we have performed calculation of the electronic structure within the DFT theory. For the calculation, we considered the fully stoichiometric parent compound $CaIr_4S_6(S_2)$. We used the crystal structure parameters described in the structure section. The full relativistic generalized gradient approximation (GGA) in the Perdew–Burke–Ernzerhof variant is used for the exchange correlation potential implemented in the full potential local orbital band-structure package (FPLO) [33,34].

The obtained electronic density of states (DOS) is presented in Figure 7. As one can see, the parent compound is a band insulator with an indirect gap of 1 eV. The orbital structure of the valence band is in the energy window from −9 eV to −1 eV and conducting in the energy window from 0 to 3 eV. It consists mainly of 5d Ir orbitals strongly hybridized with 3p S orbitals (see Figure 7).

In Figure 8, we show the orbital projected band structure. For this presentation, we use the local system of coordinates of $IrS_4(S_2)$ octahedra. The orbital structure shows that the origin of the gap is the crystal field split between e_g and t_{2g} states about 3–4 eV (see Figure 8), and the complete electron configuration of the t_{2g} states of Ir^{3+}. The obtained estimation of the crystal field splitting is comparable with the experimental obtained for Sr_2IrO_4, $Sr_3Ir_2O_7$ [35]. We would like to note that the origin of the insulating gap is different from one in compounds containing Ir^{4+} (e.g., Sr_2IrO_4, $Sr_3Ir_2O_7$ [12,36]) and Ir^{5+} (e.g., Ba_2YIrO_6 [37,38]). In the case of Ir^{4+} and Ir^{5+}, the gap stems from the splitting of t_{2g} electrons onto two configurations J = 3/2 and J = 1/2. Here, the driving mechanism is the crystal field splitting between e_g and t_{2g} electrons. Now, we turn to the question of the pairs (S_2). We compare the valence electron numbers within the DFT on a regular sulfur S^{2-} and on a sulfur in the pairs $(S_2)^{2-}$. The former sulfur corresponds to S1–S3 and the latter to S4 in the Table 1. The regular sulfur has 0.36–0.42 electron excess, while the sulfur

in a pair (S_2) 0.14, which is consistent with our discussion that the valence of the sulfur in pair (S_2) is half as much as the regular sulfur.

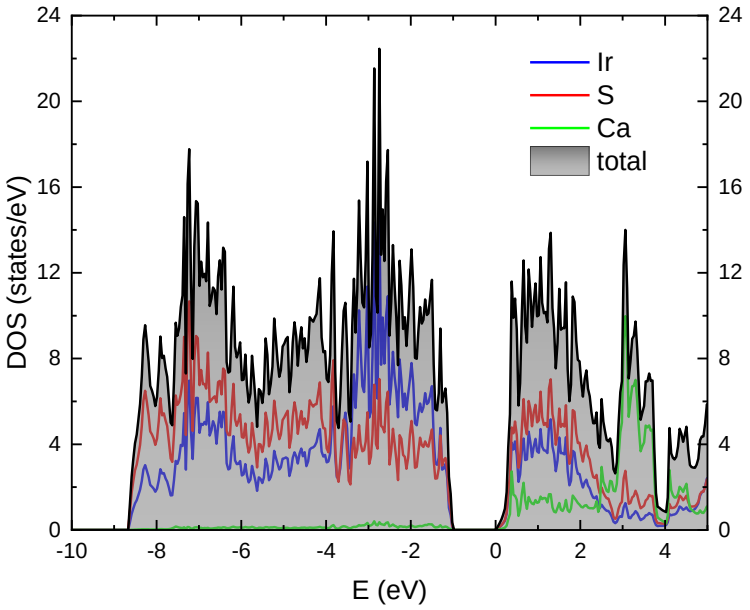

Figure 7. Total and partial density of states for each atomic species for the stoichiometric $CaIr_4S_8$.

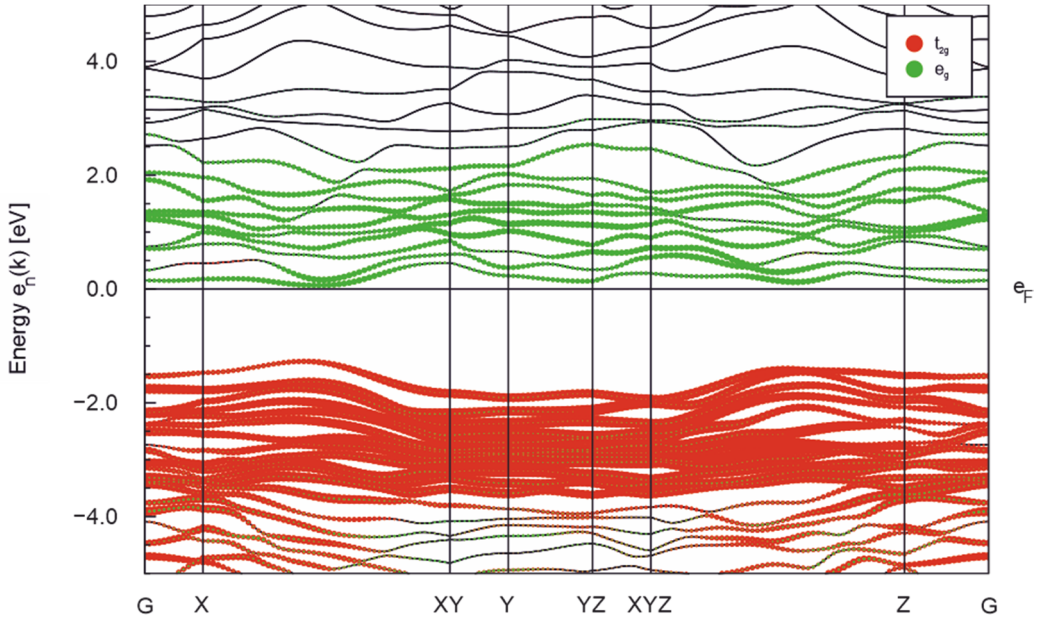

Figure 8. Electronic band structure of $CaIr_4S_8$ with orbital projected representation of 5d iridium states.

To understand the origin of the metallic state, we calculated a supercell with one Ca-vacancy per four-unit cells using VASP code. The Perdew–Burke–Ernzerhof (PBE) generalized gradient approximation (GGA) was employed [39]. The resulting DOS is presented in Figure 9. Comparison of the DOS reveals an impurity band at the top of the valence band.

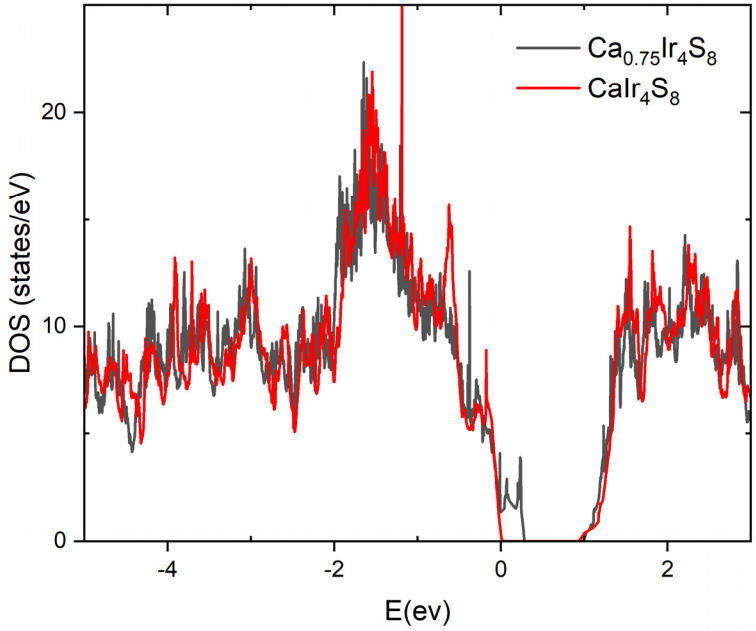

Figure 9. Comparison of DOS in $Ca_{0.75}Ir_4S_8$ and the stochiometric compound.

4. Discussion

$Ca_{1-x}Ir_4S_6(S_2)$ adopts a previously not observed structure type. Generally, in many calcium transition metal chalcogenides, the calcium-ion does not form a close-packing with the anions, likely due to its small size. Instead, calcium seems to cause one-dimensional voids through the lattices as in the title phase, $Ca_{0.75}Nb_3O_6$ [40] and $CaMn_4O_8$ [41], where the relative ratio of calcium to transition metal is small. Even in more calcium containing transition metal chalcogenides, calcium performs similarly, for example in $CaTi_2O_4$ [42] and $CaRh_2O_4$ [43]. Naturally, exceptions to this trend occur, for example the layered alpha-modification of $CaCr_2O_4$ [44]. Contrarily, only in the case of the perovskites $CaTiO_3$, where the metal ratio is 1:1, is a 3D-lattice built from close-packing of calcium and oxygen [45].

From the crystal structure determination and elemental analysis, a Ca-deficiency in the title compound is observed, which explains the presence of Ir^{4+}. The partial Ir^{4+}-state contributes to the paramagnetic behavior of $Ca_{1-x}Ir_4S_6(S_2)$. The Curie–Weiss temperature obtained from the fit is $\theta_{CW} = -31.4$ K. Despite a negative value of θ_{CW}, which is usually associated with antiferromagnetism, the susceptibility data of $Ca_{1-x}Ir_4S_6(S_2)$ show no signs of a long-range magnetic order.

Resistivity measurements show that the material is metallic. The metallic nature of $Ca_{1-x}Ir_4S_6(S_2)$ stands in strong contrast to many known iridium oxides with octahedrally coordinated iridium. Those iridates are known to have insulating properties [12]. In the case of the title compound, the conducting properties may stem from the Ca-deficiency, since DFT calculations resulted in a band-insulator for the stoichiometric parent compound. To understand the origin of the metallic state, we calculated a supercell with one Ca-vacancy per four-unit cells. Comparison of the DOS reveals impurity states on the top of the valence band.

5. Conclusions

We present the synthesis and characterization of iridium-based sulfide $Ca_{1-x}Ir_4S_6(S_2)$. Through the solid-state synthesis of CaS, iridium metal, and elemental sulfur, it was possible to obtain the compound $Ca_{1-x}Ir_4S_6(S_2)$ (x = 0.23–0.33). The material was characterized by EDXS for compositional analysis and powder X-ray diffraction measurements for the structural analysis. The structural modeling yielded a monoclinic structure within the space group $C\ 1\ 2/m\ 1$ with the lattice constants a = 15.030 (3) Å, b = 3.5747 (5) Å and c = 10.4572 (18) Å. This previously unknown structure type contains tunnels with walls of

IrS_6-octahedra that are sharing edges and vertices and are partially linked by persulfide (S-S) bridges. Within the tunnels, calcium is occupying two different, partly deficient sites. The non-stoichiometry leads to a mixed valence state of iridium, including magnetic Ir^{4+}-ions. These are responsible for the paramagnetism of the material. No long-range magnetic order is found. Electrical transport measurements on $Ca_{1-x}Ir_4S_6(S_2)$ show metallic behavior despite the strong disorder at the Ca sites. DFT calculations resulted in a band-insulator for the stoichiometric parent compound. Our calculated supercell with one Ca-vacancy per four-unit cell shows impurity states on the top of the valance band.

Supplementary Materials: The following supporting information can be downloaded at: https://www.mdpi.com/article/10.3390/electronicmat3010004/s1, File S1 the refined crystal structure model and the powder X-ray diffraction dataset.

Author Contributions: M.V. (Michael Vogl), M.V. (Martin Valldor) and S.A. synthesized and characterized the sample. S.A., M.V. (Martin Valldor) and B.B. initiated the work. D.V.E. did the band structure calculations. R.B.P. did the transport measurements. M.V. (Martin Valldor) solved the crystal structure. All the authors have contributed to the analysis of the results. S.A. and M.V. (Michael Vogl) wrote the paper with contribution from all the co-authors. All authors have read and agreed to the published version of the manuscript.

Funding: The authors acknowledge support of Deutsche Forschungsgemeinschaft (DFG) S.A. through Grant No. AS 523/4-1, M.V. and B.B. through project B01 of SFB 1143 (Project ID No. 247310070), D.V. through the project 405940956.

Data Availability Statement: The refined crystal structure model and the powder X-ray diffraction dataset presented in this study are openly available in the Supplementary Materials.

Acknowledgments: We thank Igor Morozov for useful discussions and Ulrike Nitzsche and Andrea Voß for technical assistance.

Conflicts of Interest: The authors declare no conflict of interest.

References

1. Santos-Cottin, D.; Gauzzi, A.; Verseils, M.; Baptiste, B.; Feve, G.; Freulon, V.; Plaçais, B.; Casula, M.; Klein, Y. Anomalous metallic state in quasi-two-dimensional $BaNiS_2$. *Phys. Rev. B* **2016**, *93*, 125120. [CrossRef]
2. Takeda, J.; Kodama, K.; Harashima, H.; Sato, M. Transport and Magnetic Studies of $BaCo_{1-x}Ni_xS_2$. *J. Phys. Soc. Jpn.* **1994**, *63*, 3564–3567. [CrossRef]
3. Imada, M.; Fujimori, A.; Tokura, Y. Metal-insulator transitions. *Rev. Mod. Phys.* **1998**, *70*, 1039. [CrossRef]
4. Johnston, D.C. The puzzle of high temperature superconductivity in layered iron pnictides and chalcogenides. *Adv. Phys.* **2010**, *59*, 803–1061. [CrossRef]
5. Joynt, R.; Taillefer, L. The superconducting phases of UPt_3. *Rev. Mod. Phys.* **2002**, *74*, 235–294. [CrossRef]
6. Takahashi, H.; Sugimoto, A.; Nambu, Y.; Yamauchi, T.; Hirata, Y.; Kawakami, T.; Avdeev, M.; Matsubayashi, K.; Du, F.; Kawashima, C.; et al. Pressure-induced superconductivity in the iron-based ladder material $BaFe_2S_3$. *Nat. Mater.* **2015**, *14*, 1008–1012. [CrossRef]
7. GFu, G.; Lee, J.-M. Ternary metal sulfides for electrocatalytic energy conversion. *J. Mater. Chem. A* **2019**, *7*, 9386–9405.
8. Liu, W.; Zhang, J.; Bai, Z.; Jiang, G.; Li, M.; Feng, K.; Yang, L.; Ding, Y.; Yu, T.; Chen, Z.; et al. Controllable Urchin-Like $NiCo_2$ S4 Microsphere Synergized with Sulfur-Doped Graphene as Bifunctional Catalyst for Superior Rechargeable Zn-Air Battery. *Adv. Funct. Mater.* **2018**, *28*, 1706675. [CrossRef]
9. Nagata, S.; Matsumoto, N.; Kato, Y.; Furubayashi, T.; Matsumoto, T.; Sanchez, J.P.; Vulliet, P. Metal-insulator transition in the spinel-type $CuIr_2(S_{1-x}Se_x)_4$ system. *Phys. Rev. B* **1998**, *58*, 6844. [CrossRef]
10. Croft, M.; Caliebe, W.; Woo, H.; Tyson, T.A.; Sills, D.; Hor, Y.S.; Cheong, S.W.; Kiryukhin, V.; Oh, S.J. Metal-insulator transition in $CuIr_2S_4$:XAS results on the electronic structure. *Phys. Rev. B* **2003**, *67*, 201102. [CrossRef]
11. Mizokawa, T. Electronic structure of 5 d transition-metal compounds. *J. Electron Spectrosc. Relat. Phenom.* **2016**, *208*, 78–82. [CrossRef]
12. Kim, B.J.; Jin, H.; Moon, S.J.; Kim, J.Y.; Park, B.G.; Leem, C.S.; Yu, J.; Noh, T.W.; Kim, C.; Oh, S.J.; et al. Novel $J_{eff} = 1/2$ Mott State Induced by Relativistic Spin-Orbit Coupling in Sr_2IrO_4. *Phys. Rev. Lett.* **2008**, *101*, 076402. [CrossRef]
13. Witczak-Krempa, W.; Chen, G.; Kim, Y.B.; Balents, L. Correlated Quantum Phenomena in the Strong Spin-Orbit Regime. *Annu. Rev. Condens. Matter Phys.* **2014**, *5*, 57–82. [CrossRef]
14. Singh, Y.; Manni, S.; Reuther, J.; Berlijn, T.; Thomale, R.; Ku, W.; Trebst, S.; Gegenwart, P. Relevance of the Heisenberg-Kitaev Model for the Honeycomb Lattice Iridates Na_2IrO_3. *Phys. Rev. Lett.* **2012**, *108*, 127203. [CrossRef] [PubMed]

15. Chun, S.H.; Kim, J.-W.; Kim, J.; Zheng, H.; Stoumpos, C.; Malliakas, C.D.; Mitchell, J.F.; Mehlawat, K.; Singh, Y.; Choi, Y.; et al. Direct evidence for dominant bond-directional interactions in a honeycomb lattice iridate Na_2IrO_3. *Nat. Phys.* **2015**, *11*, 462–466. [CrossRef]
16. Powell, A.; Gore, J.; Battle, P. The magnetic properties of iridium in mixed-metal oxides. *J. Alloy. Compd.* **1993**, *201*, 73–84. [CrossRef]
17. Narayanan, N.; Mikhailova, D.; Senyshyn, A.; Trots, D.M.; Laskowski, R.; Blaha, P.; Schwarz, K.; Fuess, H.; Ehrenberg, H. Temperature and composition dependence of crystal structures and magnetic and electronic properties of the double perovskites $La_{2-x}Sr_xCoIrO_6$ ($0 \leq x \leq 2$). *Phys. Rev. B* **2010**, *82*, 024403. [CrossRef]
18. Zhu, W.K.; Lu, C.-K.; Tong, W.; Wang, J.M.; Zhou, H.; Zhang, S.X. Strong ferromagnetism induced by canted antiferromagnetic order in double perovskite iridates $(La_{1-x}Sr_x)_2ZnIrO_6$. *Phys. Rev. B* **2015**, *91*, 144408. [CrossRef]
19. Cao, G.; Qi, T.F.; Li, L.; Terzic, J.; Yuan, S.J.; Delong, L.E.; Murthy, G.; Kaul, R.K. Novel Magnetism of $Ir^{5+}(5d^4)$ Ions in the Double Perovskite Sr_2YIrO_6. *Phys. Rev. Lett.* **2014**, *112*, 056402. [CrossRef] [PubMed]
20. Schaffer, R.; Lee, E.K.-H.; Yang, B.-J.; Kim, Y.B. Recent progress on correlated electron systems with strong spin–orbit coupling. *Rep. Prog. Phys.* **2016**, *79*, 094504. [CrossRef] [PubMed]
21. Nishimine, H.; Wakeshima, M.; Hinatsu, Y. Crystal structures, magnetic and thermal properties of Ln_3IrO_7 (Ln = Pr, Nd, Sm, and Eu). *J. Solid State Chem.* **2004**, *177*, 739–744. [CrossRef]
22. Brostigen, G.; Kjekshus, A.; Astrup, E.E.; Nordal, V.; Lindberg, A.A.; Craig, J.C. Redetermined Crystal Structure of FeS_2 (Pyrite). *Acta Chem. Scand.* **1969**, *23*, 2186–2188. [CrossRef]
23. Föppl, H.; Busmann, E.; Frorath, F.K. Die Kristallstrukturen von α-Na_2S_2 und K_2S_2, β-Na_2S_2 und Na_2Se_2. *ZAAC* **1962**, *314*, 12–29.
24. Tegman, R. The crystal structure of sodium tetrasulphide, Na_2S_4. *Acta Crystallogr. Sect. B* **1973**, *29*, 1463–1469. [CrossRef]
25. Yamaoka, S.; Lemley, J.T.; Jenks, J.M.; Steinfink, H. Structural chemistry of the polysulfides dibarium trisulfide and monobarium trisulfide. *Inorg. Chem.* **1975**, *14*, 129–131. [CrossRef]
26. Rietveld, H.M. A profile refinement method for nuclear and magnetic structures. *J. Appl. Cryst.* **1969**, *2*, 65–71. [CrossRef]
27. Roisnel, T.; Rodríquez-Carvajal, J. WinPLOTR: A windows tool for powder diffraction pattern analysis. *Mater. Sci. Forum* **2001**, *118*, 378. [CrossRef]
28. Petříček, V.; Dušek, M.; Palatinus, L. Crystallographic Computing System JANA2006: General features. *Z. Für Krist. -Cryst. Mater.* **2014**, *229*, 345–352. [CrossRef]
29. Jobic, S.; Deniard, P.; Brec, R.; Rouxel, J.; Drew, M.; David, W. Properties of the transition metal dichalcogenides: The case of IrS_2 and $IrSe_2$. *J. Solid State Chem.* **1990**, *89*, 315–327. [CrossRef]
30. Picard, S.; Gougeon, P.; Potel, M. Synthesis, Structural Evolution, and Electrical Properties of the Novel Mo12 Cluster Compounds $K_{1+x}Mo_{12}S_{14}$ (x = 0, 1.1, 1.3, and 1.6) with a Tunnel Structure. *Inorg. Chem.* **2006**, *45*, 1611–1616. [CrossRef]
31. Vicat, J.; Fanchon, E.; Strobel, P.; Tran Qui, D. The structure of $K_{1.33}Mn_8O_{16}$ and cation ordering in hollandite-type structures. *Acta Cryst.* **1986**, *1342*, 162–167. [CrossRef]
32. Trump, B.A.; McQueen, T.M. Structure, properties, and disorder in the new distorted-Hollandite $PbIr_4Se_8$. *J. Solid State Chem.* **2016**, *242*, 112–119. [CrossRef]
33. Koepernik, K.; Eschrig, H. Full-potential nonorthogonal local-orbital minimum-basis band-structure scheme. *Phys. Rev. B* **1999**, *59*, 1743–1757. [CrossRef]
34. FPLO-18 Package. 2018. Available online: http://www.fplo.de (accessed on 19 November 2021).
35. Sala, M.M.; Rossi, M.; Al-Zein, A.; Boseggia, S.; Hunter, E.C.; Perry, R.S.; Prabhakaran, D.; Boothroyd, A.T.; Brookes, N.; McMorrow, D.; et al. Crystal field splitting in $Sr_{n+1}IrnO3_{n+1}$(n = 1, 2) iridates probed by x-ray Raman spectroscopy. *Phys. Rev. B* **2014**, *90*, 085126. [CrossRef]
36. Kim, B.J.; Ohsumi, H.; Komesu, T.; Sakai, S.; Morita, T.; Takagi, H.; Arima, T. Phase-Sensitive Observation of a Spin-Orbital Mott State in Sr_2IrO_4. *Science* **2009**, *323*, 1329–1332. [CrossRef]
37. Dey, T.; Maljuk, A.; Efremov, D.V.; Kataeva, O.; Gass, S.; Blum, C.G.F.; Steckel, F.; Gruner, D.; Ritschel, T.; Wolter, A.U.B.; et al. Ba_2YIrO_6: A cubic double perovskite material with Ir^{5+} ions. *Phys. Rev. B* **2016**, *93*, 014434. [CrossRef]
38. Kim, B.H.; Efremov, D.V.; Brink, J.V.D. Spin-orbital excitons and their potential condensation in pentavalent iridates. *Phys. Rev. Mater.* **2019**, *3*, 014414. [CrossRef]
39. Perdew, J.P.; Burke, K.; Ernzerhof, M. Generalized Gradient Approximation Made Simple. *Phys. Rev. Lett.* **1997**, *78*, 1396. [CrossRef]
40. Hibble, S.J.; Cheetham, A.K.; Cox, D.E. $Ca_{0.75}Nb_3O_6$: A Novel Metal Oxide Containing Niobium-Niobium Bonds. Characterization and Structure Refinement from Synchrotron Powder X-ray Data. *Inorg. Chem.* **1987**, *26*, 2389–2391. [CrossRef]
41. Barrier, N.; Michel, C.; Maignan, A.; Hervieu, M.; Raveau, B. $CaMn_4O_8$, a mixed valence manganite with an original tunnel structure. *J. Mater. Chem.* **2005**, *15*, 386–393. [CrossRef]
42. Bertaut, E.F.; Blum, P. Détermination de la Structure de Ti_2CaO_4 par la Méthode Self-Consistante d'Approche Directe. *Acta Crystallogr.* **1956**, *9*, 121–126. [CrossRef]
43. Yamaura, K.; Huang, Q.; Moldovan, M.; Young, D.P.; Sato, A.; Baba, Y.; Nagai, T.; Matsui, Y.; Takayama-Muromachi, E. High-Pressure Synthesis, Crystal Structure Determination, and a Ca Substitution Study of the Metallic Rhodium Oxide $NaRh_2O_4$. *Chem. Mater.* **2005**, *17*, 359–365.

44. Pausch, H.; Müller-Buschbaum, H. Die Kristallstruktur von α-$CaCr_2O_4$. *Z. Anorg. Allg. Chem.* **1974**, *405*, 113–118.
45. Sasaki, S.; Prewitt, C.T.; Bass, J.D.; Schulze, W.A. Orthorhombic perovskite $CaTiO_3$ and $CdTiO_3$: Structure and space group. *Acta Cryst. C* **1987**, *43*, 1668–1674. [CrossRef]